Effects of oxygen index on soot production and temperature in an ethylene inverse diffusion flame

F. Escudero [a,b], A. Fuentes [a,*], R. Demarco [a], J.-L. Consalvi [c], F. Liu [d], J.C. Elicer-Cortés [b], C. Fernandez-Pello [e]

[a] Departamento de Industrias, Universidad Técnica Federico Santa María, Av. España 1680, Valparaíso, Chile
[b] Departamento de Ingeniería Mecánica, Universidad de Chile, Av. Beauchef 851, Santiago, Chile
[c] Aix-Marseille Université, IUSTI/UMR CNRS 7343, 5 rue E. Fermi, 13453 Marseille Cedex 13, France
[d] Black Carbon Metrology, Measurement Science and Standards, National Research Council of Canada, 1200 Montreal Road, Ottawa, Ontario K1A 0R6, Canada
[e] Department of Mechanical Engineering, University of California, Berkeley, CA 94720, USA

ARTICLE INFO

ABSTRACT

An experimental study was conducted to investigate the effects of the Oxygen Index (OI) in an ethylene laminar inverse diffusion flame (IDF). The OI was varied from 21% to 37% and its influence was measured in terms of the flame height, soot volume fraction, soot temperature and radiant fraction. The stoichiometric flame height was measured by the spontaneous emission of CH* radicals and was found to decrease when the OI increases. In contrast, the luminous flame height increases with OI because soot can still form and grow beyond the reaction zone. Radial profiles of soot volume fraction and soot temperature were obtained by means of a Modulated Absorption/Emission (MAE) technique. The line-of-sight intensities, integrated along the optical path and captured by ECCD camera at two wavelengths were inverted using deconvolution and regularization techniques in order to obtain radial profiles of soot volume fraction and temperature. The increase in OI enhances soot volume fraction due to higher temperatures and soot formation rates. Both the local and integrated soot quantities increase with OI. The radiant fraction of IDF increases with the OI in a similar way to the integrated soot volume fraction.

© 2015 Elsevier Inc. All rights reserved.

1. Introduction

Combustion is a very complex phenomenon and has been studied for many decades. However, complete understanding of combustion processes in turbulent flames remains a challenge due to the large number of simultaneous processes involved. The axisymmetric laminar diffusion flame configuration has often been used as a valuable model to gain fundamental insights into the complex phenomena occurring in turbulent flames. These laminar flames are of great interest because they are sufficiently stable and repeatable to allow non-simultaneous measurements of various quantities, such as velocity, temperature, and species concentrations, to probe the effects of various parameters on flame properties, including but not restricted to the fuel and oxidizer stream velocities, fuel dilution, and oxidizer compositions. Depending on the flame characteristics, soot may or may not be completely consumed within the flame. Emissions of soot from flames and combustion systems have been identified harmful to human health

and the environment [1]. It is interesting to mention that in some industrial applications, in which the direct flame radiation is used to heat the secondary fluid, it is often desirable to enhance soot formation in flames to maximize radiation heat transfer from flames yet to avoid emissions of soot from such combustion devices. The amount of released soot depends on the competition between soot formation and soot oxidation processes within the flame.

Despite the significant progress in the last few decades towards soot formation processes, the key steps in soot inception remain elusive [2]. The inverse diffusion flame (IDF) is an interesting flame configuration to investigate particularly the soot inception process. IDFs are similar to normal diffusion flames (NDFs) in terms of the flame structure, but the roles of fuel and oxidizer are exchanged: an oxidizer flow is surrounded by a fuel flow in an IDF and soot escapes from the reaction zone un-oxidized allowing its study in the early stages of formation [3]. The combustion process in an IDF resembles that in an under-ventilated NDF and is highly relevant to flames or fires under fuel rich conditions.

There have been extensive studies of NDFs. However, only few works have been reported in the literature concerning IDFs. The concept of the inverse diffusion flame was introduced vaguely by Friend [4] in the early 20s in a single sentence. Burke and

---

Nomenclature

a	buoyancy acceleration of a fluid parcel within the flame (m s^{-2})
C_2	second constant of Planck's equation (m K)
C_λ	absorption function (–)
Fr	Froude number (–)
f_s	soot volume fraction (ppm)
HAB	height above the burner (m)
h_f	flame height (m)
HRR	heat release rate (W)
I_λ	spectral radiation intensity of the flame (W sr^{-1} m^{-3})
I_λ^{bb}	blackbody spectral radiation intensity of the flame (W sr^{-1} m^{-3})
J_λ	local emission of the flame (W sr^{-1} m^{-4})
l	local position along the line-of-sight within the flame (m)
l_0	beginning of the line-of-sight of the flame (m)
l_1	end of the line-of-sight of the flame (m)
N	number of annular elements of the discretized flame (–)
Q	volumetric flow rate (m^3 s^{-1})
q''	vertical distribution of heat flux measured by the radiometer (W m^{-2})
R	distance between the radiometer and the axis of the flame (m)
r	radial position from the flame axis (m)
R_f	flame radius (m)
T_{ad}	adiabatic temperature of the flame (K)

t_{res}	residence time of a fluid parcel to reach the flame height (s)
V_f	fuel velocity at the burner exit (m s^{-1})
y	abscissas coordinate of the projected data (m)
z	vertical distance from the burner exit surface (m)

Greek symbols

β	integrated soot volume fraction (ppm m^2)
κ_λ	spectral absorption coefficient (m^{-1})
λ	wavelength (m)
τ_λ	fraction of transmitted light (–)
$\Phi_{overall}$	overall equivalence ratio, defined as the fuel-to-air ratio divided by the stoichiometric fuel-to-air ratio at the burner exit (–)
χ_r	radiant fraction (–)

Acronyms

FWHM	full width at half maximum
IDF	inverse diffusion flame
LOSA	line-of-sight attenuation
MAE	Modulated Absorption/Emission
NDF	normal diffusion flame
OI	oxygen index
OP	Onion-Peeling
PAH	polycyclic aromatic hydrocarbons

Schumann [5] reported the measured heights of some IDFs but without specific details. More recently, there have been more studies about this type of flames. Wu and Essenhigh [6] mapped inverse methane flames by varying the air and fuel velocities and identified six different regimes with stable and unstable flames and emitting more or less soot depending the flow conditions. Lee et al. [7] identified a similar kind of map for ethylene flames adding three more kind of regimes. They also identified the reaction zone, soot particles and the degree of soot maturation by means of carbon to hydrogen ratio (C/H ratio) and morphology of soot samples. Kaplan and Kailasanath [8] made direct numerical simulations for different quotients between air and fuel velocities for NDFs and then compared them with IDFs with the same velocities. They found that under the same conditions IDFs produce much less soot than NDFs because the surface growth rate is lower in IDFs due to the unfavorable temperature and stoichiometric conditions for soot inception. Blevins et al. [9] confirmed the hypothesis that soot of IDFs is similar to the one of NDFs by collecting samples of exhaust soot and analyzing its morphology. Mikofski et al. [10,11] analyzed the structure and heights of methane and ethylene flames varying the air flow rate. They studied quantitatively the temperature of flames and qualitatively the concentrations of soot, PAH and OH* radicals to understand the soot formation mechanisms in these flames, which were found similar to the mechanisms in NDFs. They also found that heights of reaction zone of the flames follow the theory of Roper for circular port burners. Macko et al. [12] made extinction measurements to obtain soot concentrations and found that they were about an order of magnitude lower than those in NDFs. Demarco et al. [13] studied numerically IDFs with OI of 21% focusing on radiative heat transfer. They showed that radiant fractions are much lower than those observed in NDFs and the contribution of soot to radiation is lower than the contribution of gaseous radiant species.

An effective way to alter the relative importance of soot production and oxidation mechanisms, and therefore the radiative properties of a flame, is to vary the oxygen index (OI) defined as the mole concentration of oxygen in the oxidizer stream containing a mixture of oxygen and nitrogen. Recently, Jung et al. [14] studied the effects of OI in ethylene IDFs. They measured the heights and temperature of the flame and the concentrations of PAHs and soot. They also measured the C/H ratio to evaluate the degree of carbonization. In this study new experimental data are obtained as a function of OI, from 21% to 37%, in a standard inverse flame burner. Non-intrusive diagnostics were carried out in order to obtain radially resolved profiles of soot temperature and soot volume fraction, the radiant fraction and the height of the reaction zone. These results are valuable addition to the existing experimental results obtained in similar NDFs conditions for validation of numerical models of soot formation and growth.

2. Experimental methodology

In the following section the experimental setup and conditions used in the study are presented. Also the experimental procedure to obtain soot volume fraction, soot temperature, flame height and radiation heat flux is described.

2.1. Inverse flame burner and experimental conditions

The IDF investigated in this study was produced with a similar co-annular inverse flame burner used previously in other studies by Blevins et al. [9], Mikofski et al. [10,11] and Macko et al. [12]. Basically, the inverse flame burner consists of three concentric tubes. The inner diameters of the tubes were 10, 30 and 64 mm for the oxidizer, fuel, and inert flows, respectively. The fuel tube and the inert annulus contain a honeycomb structure to smooth the flow. The fuel used was pure ethylene and the inert gas was nitrogen to prevent secondary flames from forming between the fuel and the ambient air. For OIs lower than 21% the flame became

unstable with more flickering. For this reason, only the OI range between 21% and 37% was studied. To achieve the desired OI, normal air (assumed to be 21% oxygen and 79% nitrogen) supplied by a compressor was doped by the required amount of pure oxygen. The volumetric ethylene flow rate was kept constant at 2.7 slpm for all conditions following the conditions used by Mikofski et al. [10,11] and Macko et al. [12], where only an OI of 21% (air) was considered. The flow rates of different streams (oxidizer, inert and fuel) were controlled by thermal mass flow controllers from Brooks Instruments, Series SLA5850 (cf. Fig. 1). The flow conditions in the present experiments are summarized in Table 1.

Heat release rate (HRR) was calculated using the heat of combustion of ethylene assuming that air reacts completely. The overall equivalence ratio $\Phi_{overall}$ was defined as the fuel-to-air ratio divided by the stoichiometric fuel-to-air ratio considering the flows at the burner exit. This value is always higher than 1 so the global mixture is always fuel rich. The adiabatic temperature T_{ad} for each condition was obtained by using STANJAN [15]. For buoyancy-controlled flames the acceleration can be considered as a constant. Santoro et al. [16] showed that for different NDFs the buoyancy acceleration was approximately 32.1 m/s² so this value was used for ambient conditions. As the buoyancy acceleration increases with the OI, the acceleration for different OIs was estimated as the product of the ambient condition acceleration with the ratio of adiabatic temperature of each OI condition relative to that of the ambient condition [14]. Finally, the Froude number (Fr) was calculated as proposed by Turns [17] for a laminar jet flame. All flames were found buoyancy-controlled with Froude numbers lower than 0.3 under all conditions.

2.2. Optical arrangement

A schematic of the experimental set-up is shown in Fig. 1. A diode laser of 660 nm operated at 1500 mA was used as a light source for line-of-sight attenuation (LOSA) to obtain soot volume fraction measurements. The 100 mm diameter beam passes through the flame and then is focused by an achromatic lens (300 mm focal length). On the path of the beam, a neutral filter is set to avoid saturating the camera, a pinhole to eliminate unwanted noise and a 660 nm (10 nm FWHM) band pass filter to avoid interference sources. A monochromatic CCD camera was devoted to capture LOSA images, with 1038 × 1384 pixels on each image with a resolution of 0.06 × 0.06 mm² for each pixel element. During each experiment, the laser was pulsed at a frequency of 1 Hz by means of an external pulse generator. This procedure produced modulated images of emission and absorption from soot particles, as proposed by Jenkins and Hanson [18], allowing to take images with laser on and off, with and without flame, decreasing the error in the soot volume fraction measurements.

Another ECCD (Andor Lucas R) camera was devoted to capture flame emission images, with 1002 × 1004 pixels on each image and a pixel resolution of 0.14 × 0.14 mm². A filter wheel was set in front of the camera allowing to rapidly changing the filter. Three band pass filters were used: a 431 nm (10 FWHM) to CH* spontaneous emission measurements in order to identify the reaction zone of the flame [19], a 660 nm (10 FWHM) and a 800 nm (10 FWHM) for flame emissions to evaluate the local soot temperature based on the two-color pyrometry principle. A PENTAX f/1.4 12-mm focal length lens was mounted on each camera focused at
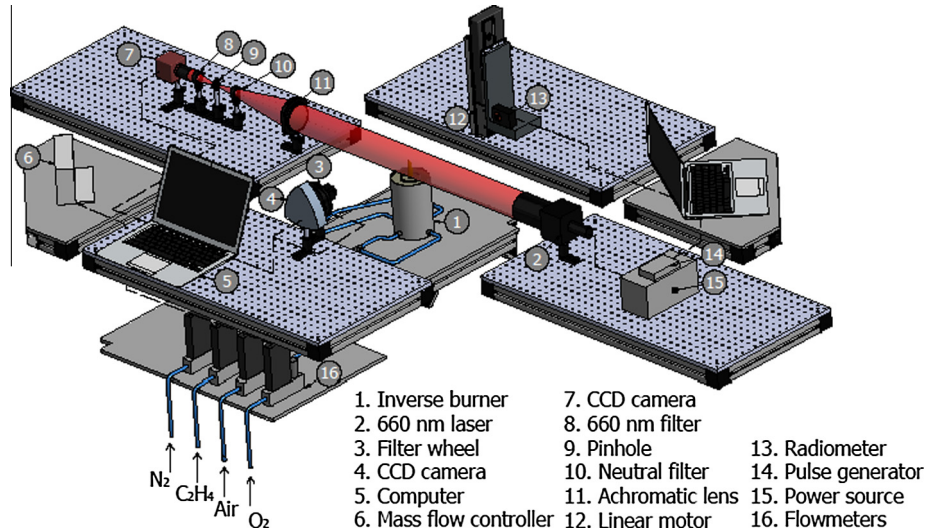

1. Inverse burner   **7.** CCD camera
2. 660 nm laser   **8.** 660 nm filter
3. Filter wheel   **9.** Pinhole   **13.** Radiometer
4. CCD camera   **10.** Neutral filter   **14.** Pulse generator
5. Computer   **11.** Achromatic lens   **15.** Power source
6. Mass flow controller   **12.** Linear motor   **16.** Flowmeters

Fig. 1. Schematic of the experimental apparatus.

Table 1
Experimental conditions.

OI (%)	Q_{ox} (slpm)	Q_{air} (slpm)	Q_{O_2} (slpm)	HRR (W)	$\Phi_{overall}$ (−)	T_{ad} (K)	a (m/s²)	Fr (−)
21	2.2	2.2	0	142.7	17.51	2403	32.10	0.278
23	2.2	2.14	0.06	156.3	16.03	2495	33.33	0.267
25	2.2	2.09	0.11	169.9	14.79	2575	34.40	0.257
27	2.2	2.03	0.17	183.5	13.73	2646	35.35	0.249
29	2.2	1.98	0.22	197.1	12.82	2709	36.20	0.244
31	2.2	1.92	0.28	210.6	12.02	2767	36.97	0.239
33	2.2	1.87	0.33	224.2	11.33	2820	37.67	0.234
35	2.2	1.81	0.39	237.8	10.71	2868	38.32	0.230
37	2.2	1.75	0.45	253.0	10.16	2919	38.99	0.232

the burner plane of symmetry. For each experimental condition at least 100 images were taken to improve signal-to-noise ratio for emission and LOSA measurements.

2.3. Radiative flux and flame height

Radiation measurements were obtained with a Medtherm 64-0.2-15 Schmidt–Boelter gauge, fitted with a 150° angle sapphire window in order to eliminate any convective heat readings. The radiometer was mounted over a linear stage motor moving at a constant velocity of 3 mm/s, parallel to the flame axis at a distance of 150 mm, obtaining radiative heat flux measurements at different heights from 30 mm below to 120 mm above the burner exit surface. Flame height measurements are useful to characterize the inverse laminar diffusion flame since it is an important parameter to validate numerical models and to estimate residence times of soot particles inside the flame. To determine the reaction zone of the flame, CH* spontaneous emission images were processed by using the segmentation method of Ko et al. [20].

2.4. Soot production and temperature radial profiles

From LOSA measurements the fraction of transmitted light (τ_λ) passing through the flame at each height above the burner was obtained following the methodology of Jenkins and Hanson [18]. This quantity is related to the spectral absorption coefficient (κ_λ) as follows:

$$-\ln(\tau_\lambda) = 2\int_y^{R_f} \frac{\kappa_\lambda(r)r}{\sqrt{r^2 - y^2}}dr \tag{1}$$

where r is the radial coordinate within the flame, y is the abscissas coordinate of the projected data and R_f is the flame radius. This is a type of Abel's integral equation [21] and it can be solved using an Onion-Peeling (OP) deconvolution algorithm [22], which consists in discretizing the flame cross section into N annular elements where the properties are assumed constant inside each ring. The equation system is ill-posed because the solution is highly sensitive to small perturbations in the projected data, so a zero-order Tikhonov regularization technique [23] is applied, where the original system is replaced by a less ill-posed system. This procedure needs a regularization parameter, which controls the degree of regularization. This parameter can be found using the L-Curve criterion [24], smoothing the solution without significantly deteriorating the quality of the solution. By solving the matrix system, the local absorption coefficient can be calculated and thus the local soot volume fraction as $f_s(r) = \lambda\kappa_\lambda(r)/C_\lambda$ [25] where C_λ was determined with the correlations given in [26].

To calculate the local soot temperature, flame emissions at two wavelengths are measured. Absorption and emission of radiation along a line-of-sight across the flame is described by the radiative transfer equation:

$$\frac{dI_\lambda}{dl} + \kappa_\lambda(l)I_\lambda = J_\lambda(l) \tag{2}$$

where I_λ is the spectral radiation intensity, $J_\lambda(l) = \kappa_\lambda(l)I_\lambda^{bb}$ represents the local emission of the flame, dl is the differential distance travelled by the light and l represents the local position along the line-of-sight within the flame under consideration and I_λ^{bb} is the blackbody spectral intensity given by Planck's equation. The solution to the above radiative transfer equation, written explicitly in terms of the radial coordinate of the flame $r = \sqrt{l^2 + y^2}$ is:

$$I_\lambda(y) = \int_{l_0(y)}^{l_1(y)} J_\lambda\left(\sqrt{l^2 + y^2}\right)\exp\left(-\int_l^{l_1(y)}\kappa_\lambda\left(\sqrt{l^2 + y^2}\right)dl'\right)dl \tag{3}$$

where the terms $l_0(y) = -\left(R_f^2 - y^2\right)^{1/2}$ and $l_1(y) = \left(R_f^2 - y^2\right)^{1/2}$ represents the beginning and the end points of the line-of-sight for a flame of radius R_f, respectively. This equation can be discretized and solved to obtain $J_\lambda(r)$ following the work of Liu and Jiang [27]. This procedure can be applied to measure line-of-sight intensities at any two wavelengths. As the soot volume fraction is a physical property, it was considered independent of the wavelength. Once the blackbody intensities at the two wavelengths are obtained, the local temperature can be derived from their ratio, following the work of Jenkins and Hanson [18].

$$T(r) = \frac{C_2\left(\frac{1}{\lambda_2} - \frac{1}{\lambda_1}\right)}{\ln\left(\frac{C_{\lambda_2}}{C_{\lambda_1}}\frac{J_{\lambda_1}(r)}{J_{\lambda_2}(r)}\left(\frac{\lambda_1}{\lambda_2}\right)^6\right)} \tag{4}$$

3. Results and discussion

3.1. Flame height analysis

The CH* spontaneous emission images are used to determine the stoichiometric flame height, which is defined as the distance between the burner exit surface and the axial location of the maximum CH* intensity. A typical image taken by the CCD camera is shown in Fig. 2a for an OI of 37%. Two important zones can be identified: an inner reaction zone and an outer visible luminous zone. The first one is important for numerical modelling and the second one to calculate the residence time of soot particles inside the luminous flame height. To identify both zones, a proper threshold was used to identify the reaction zone meanwhile a less critical threshold was adopted in order to detect the contours of luminous region [18]. Fig. 2b shows the luminous and reaction zone height for the different OIs analyzed. At 21% of OI the reaction zone height is approximately 21.5 mm, which is consistent with the results of Mikofski et al. [10] under the same conditions. The decrease in the reaction zone height was from 21.4 mm at 21% to 19.3 mm at 37%, which is only about 10% and much smaller than that observed in NDFs [28].

The reaction zone height decreases almost linearly as the OI increases. The opposite trend is observed for the luminous flame height, which increases with increasing OI but in a sub-linear fashion. Clearly, the variation of the reaction zone height with OI follows a similar behavior as that observed in NDFs. However, the variation of the luminous flame height of IDFs with OI is in contrast to that of NDFs. The increase in luminous flame height with OI can be explained by the fact that the temperature of the soot particle that escapes from the reaction zone is enhanced leading to higher soot radiation in the visible. The OI affects directly this behavior and controls the oxidation of soot particles, decreasing relatively the emission and obtaining a plateau for higher OI.

The error bars presented in Fig. 2b were estimated based on a sensitivity analysis of the threshold value used in the segmentation model. Once a threshold value was chosen, it was varied by 40% to quantify the changes in flame height. This analysis showed that the flame height in both cases was weakly sensitive to changes in the threshold value and for all cases the change in flame height was less than 5.5%, with higher sensitivities at lower OIs.

3.2. Residence time

The right axis of Fig. 2b shows the residence times for a fluid parcel from the burner exit surface to either the reaction zone height or the luminous flame tip calculated assuming a constant buoyancy-acceleration for each condition as
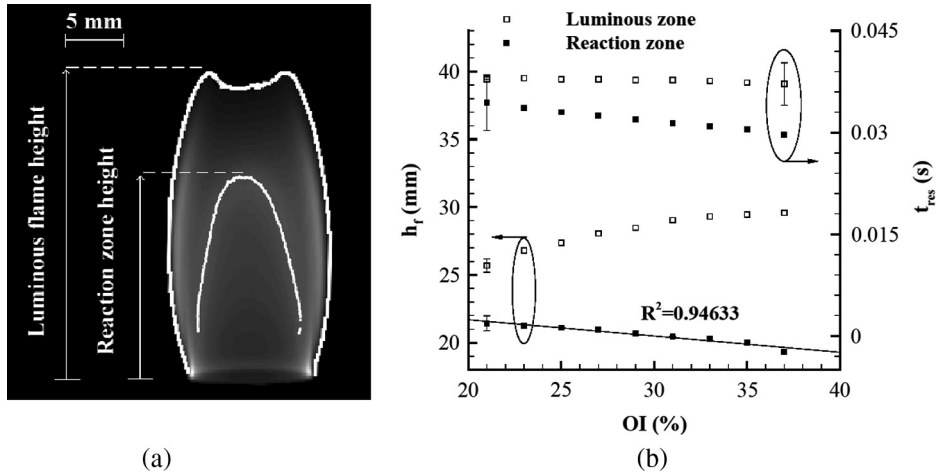
Fig. 2. (a) Visible image obtained from CH* emissions for 37% of OI. (b) Reaction zone and luminous flame heights (left axis) and residence times (right axis) as a function of OI.

$$t_{res} = \frac{1}{a}\left(\sqrt{2ah_f + V_f^2} - V_f\right) \tag{5}$$

where a is the buoyancy-acceleration given in Table 1 for each condition, V_f is the fuel velocity at the burner exit and h_f is the flame height. All residence times were between 30 and 40 ms for all conditions of this study. The maximum errors are shown, which were calculated based on the uncertainties of flame height.

In Fig. 2b it is possible to observe that the residence times based on the stoichiometric flame height decreases with increasing OI. This happened due to two effects: the increase in the acceleration due to higher buoyant effects and the decrease in flame height as the OI increases. However, beyond the reaction zone the soot particles can still grow if the temperature is sufficiently high [14].

Therefore, it is better to use the luminous height to estimate residence times of soot particles. In this case, the luminous height increases with OI, tending to increase residence time, and acceleration tends to decrease it, so these two competing effects somewhat cancel out and the residence time to reach the luminous flame height remains approximately constant with a value about 37–38 ms for all conditions studied. As this residence time does not vary with OI, the effects of other parameters on soot can be directly compared.

3.3. Soot volume fraction and temperature

The effects of OI on soot volume fraction and soot temperature are presented in Fig. 3. As the reaction zone height does not vary
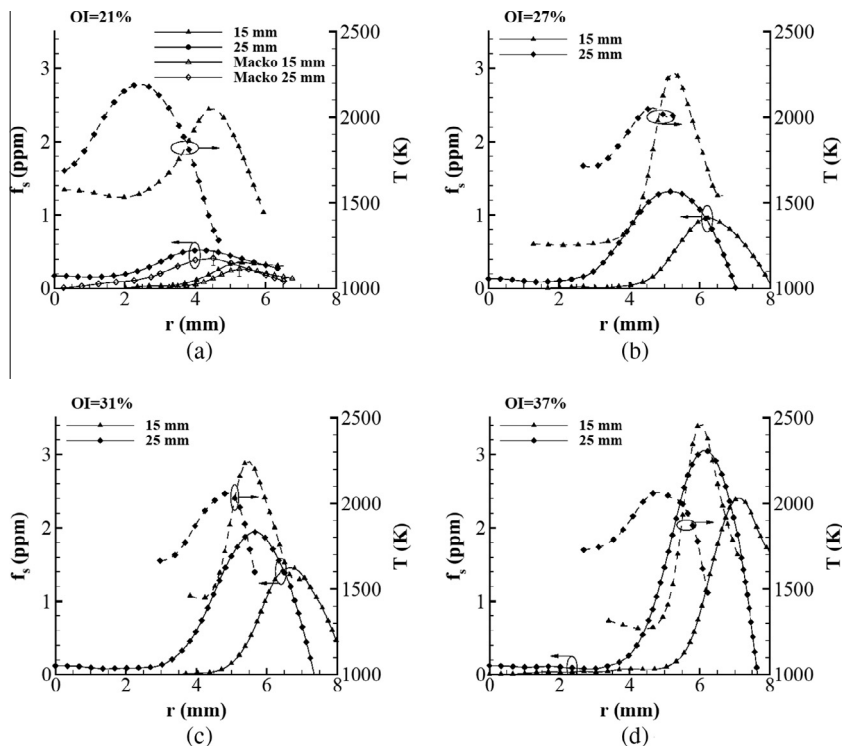

Fig. 3. Radial profiles of soot volume fraction (continuous) and soot temperature (dashed) at different HAB for four OI: (a) OI = 21%, (b) OI = 27%, (c) OI = 31% and (d) OI = 37%. For OI = 21% the dotted line represents the experimental results of Macko et al. [12].

significantly, the same heights were chosen for the different OIs for comparison purposes.

As observed in the Fig. 3, soot concentration increases with OI at each height. For an OI of 21% measured soot volume fractions at 15 and 25 mm above the burner were compared with those obtained by Macko et al. [12] under the same experimental conditions. A good agreement was observed. The peaks of soot volume fraction are about 0.5 ppm for lower OIs and almost 3.5 ppm for an OI of 37%. When the oxygen content in the oxidizer stream is increased there are two mechanisms affecting the soot production. There is an increase in the flame temperature which leads to an increase in soot formation rates and fuel pyrolysis, thus nucleation and surface growth rates are higher and the flame is more likely to produce higher soot concentrations. On the opposite, increasing the OI promotes oxidation mechanisms because of the higher temperature and concentrations of oxidative species, which tend to decrease the soot volume fraction. Those effects can be clearly observed in NDFs by analyzing radial soot profiles at different heights above the burner (HABs) [28]. However, in IDFs the oxidation mechanism is less important because soot is formed in the fuel-side and it moves outside the flame to cooler regions without passing through an oxidative environment [3]. For this reason, soot volume fraction increases with increasing OI in a different manner as observed in NDFs.

As observed soot profiles tend to increase with the radial position, reach a maximum and then decrease quickly close to the peak of temperature. The radial position of the maximum approaches the flame axis with increasing distance from the burner exit. Nevertheless it never reaches the axis because soot moves outwards the flame, leading to an open tip. This is different from NDFs (under the smoke point), where the peak of soot volume fraction moves to the flame axis at higher distance from the burner exit, forming a closed tip flame. Although the reaction zone height is about 20–22 mm for all flames, soot volume fraction keeps increasing above this height, so soot is still being formed and experiencing growth beyond the reaction zone, if the temperature is sufficiently high (>1600 K) [14].

For soot temperature radial profiles the general trend is that soot temperature increases as the OI increases. As a consequence, the rates of soot formation are enhanced, leading to higher soot volume fractions. Generally, soot temperature also increases radially to the reaction zone, reaching a maximum at a radial position between 4 and 6 mm, next to the radial position where the maximum soot volume fractions also occur. The temperatures in this region is about 2000–2500 K at $z = 15$ mm (z is the vertical distance from the burner exit surface) and 1800–2100 K for $z = 25$ mm. Therefore, the temperatures are sufficiently high for soot formation processes to take place. In all cases, the peak soot temperatures are located just inside the soot volume fraction peaks, as expected from the structure of an inverse diffusion flame.

In order to quantify the measurement uncertainties, a typical error propagation equation was used. For soot volume fraction, the uncertainties of C_λ, κ_λ and λ were considered and the error was calculated based on the work of Fuentes et al. [29], giving a maximum uncertainty of 30% for soot volume fraction. For soot temperature, a similar analysis was conducted, considering uncertainties of λ_1, λ_2 and of the quotient between flame emissions $J_{\lambda_1}/J_{\lambda_2}$. The analysis was based on the work of Liu et al. [30] and a maximum uncertainty of 16%, corresponding to 350 K for high temperatures, was obtained.

3.4. Integrated soot volume fraction

In order to quantify the global amount of soot at a given z, the integrated soot volume fraction β is calculated as:

$$\beta = \int_0^{2\pi} \int_0^R f_s(r) r \, dr \, d\theta \tag{6}$$

This parameter serves as an indicator of the evolution of soot production through the flame height. This equation can be easily discretized and calculated. Fig. 4a shows the computed values of β as a function of z for different OIs. A clear trend is observed showing increased soot production with increasing OI. The total amount of soot varies from 0.9 to 3 ($\times 10^{-10}$ m^2), which is lower than that observed in NDFs for lower OIs, consistent with the experimental [12] and numerical [8,13] studies of this type of flames.

Fig. 4b shows the maximum of β (left axis) and the position at which occurs (right axis) as a function of the OI. The error bars were obtained based on the error of soot volume fraction. Although the formation mechanisms are enhanced with the OI and the acceleration and residence times are also affected, the position of the maximums occur at almost a constant z of about 38.2 mm, following the same behavior as in NDFs [28]. The increase in the integrated soot volume fraction with OI is approximately linear in the range of OI analyzed in this study.

Angrill et al. [31] quantified the rates of formation and oxidation of different NDFs by means of the slope of curves of $f_s(r = 0)$ (soot volume fraction at the axis of the flame) as a function of z. In the case of the analyzed IDFs, at the flame axis there are low quantities of soot so the information of those curves is not useful. For this reason, the same idea was used to plot Fig. 4c [31] but using the curves presented in Fig. 4a which also represents the global evolution of soot production. Before reaching the maximum of curves of Fig. 4a the slope is positive, which indicates dominance of soot formation over soot oxidation. After the maximum, the oxidation processes become dominant. Fig. 4c shows the slopes at the left (positive sign, formation predominates) and right (negative sign, oxidation predominates) of the maximums of Fig. 4a. The error bars correspond to the largest error and were calculated from the error of soot volume fraction. The slopes of the soot formation dominating zone increase linearly with the OI, which corroborates that increasing the OI enhance soot formation mechanisms in IDFs which tends to increase the amount of soot. In contrast, the slopes of the oxidation predominant zone do not show a clear behavior and tend to keep approximately constant. Based on this, the oxidation rates do not increase appreciably with the OI as observed in NDFs, which is consistent with the large amount of un-oxidized soot particles escaping from the tip of the flames.

3.5. Radiant fraction

The radiant fraction is the ratio between the total radiation loss and the HRR of the flame. To calculate the total radiation loss for each condition, vertical distribution of heat flux (q'' in W/m^2) is measured by means of a radiometer. Then, the radiant fraction is computed as:

$$\chi_r = \frac{2\pi R \int_{z_1}^{z_2} q''(z) dz + \pi R^2 q''(z_1) + \pi R^2 q''(z_2)}{HRR} \tag{7}$$

where R is the distance between the radiometer and the axis of the flame, z_1 and z_2 are the heights of the beginning and ending of the measurement, respectively. The radiation emitted by the flame is assumed to be received for the surface of a cylinder centered at the flame axis of radius R and height z_2-z_1. The HRR for each OI is summarized in Table 1.

Fig. 4d shows the radiant fraction as a function of the OI with the uncertainties calculated considering a statistical error and an error analysis for a Schmidt–Boelter radiometer [32]. Clearly, the radiant fraction increases almost linearly with the OI in the range studied showing the same trends observed in NDFs. Also, the total radiation loss obtained in IDFs is lower than that of typical NDFs,
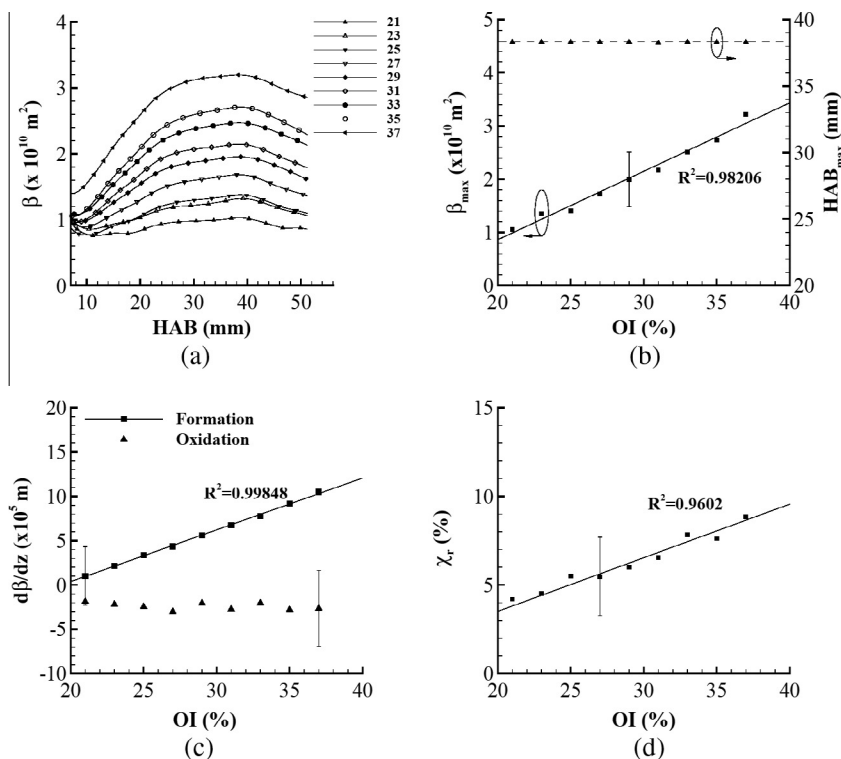
Fig. 4. (a) Vertical distribution of β as a function of the height above the burner. (b) β_{max} (squares) and HAB_{max} (triangles) as a function of the OI. The dashed line corresponds to the averaged value HAB_{max} (38.2 mm) where the maximum occurs. (c) Slope of β to quantify rates of oxidation and formation, as a function of OI. (d) Radiant fraction as a function of the OI.

which shows that the radiation heat transfer is directly linked with the amount of soot within the flame, because in NDFs the amount of soot is generally much larger, for similar flow conditions. Consequently, the radiation loss released by NDFs is more significant. This is in line with the results of simulations reported by Demarco et al. [13].

4. Conclusions

An experimental study was carried out in order to evaluate the effects of oxygen index on radiation, geometry, soot temperature, and soot production in IDFs generated in a co-annular three port burner. The reaction zone height decreases from 22.3 to 21.4 mm from 21% to 37% of OI, which is less pronounced than in some NDFs presented in the literature. The luminous flame height is higher than the reaction zone height because soot formation and growth processes continue beyond the reaction zone and the soot oxidation processes are nearly absent.

Soot temperature was found to be between 1800 and 2500 K near the radial positions of the peak soot volume fractions. These temperatures are sufficiently high for soot formation to occur beyond the reaction zone height. Soot volume fraction increases with increasing OI because the soot formation processes are enhanced, but the oxidation processes are not significantly affected in the range of OI studied, confirming that this flame configuration allows decoupling oxidation and formation processes, which is valuable information to validate numerical or theoretical models of soot inception and surface growth in diffusion flames. The peak of integrated soot volume fraction increases linearly with OI and the axial position of the peaks remains unaffected by the OI.

Radiation loss of the flame is enhanced with the OI with a linear behavior, in a similar way to the integrated soot volume fraction. As the soot loading within the flame increases, the radiation emitted by the flame also increases. The radiant fraction of the IDFs

studied is lower than that in the NDFs of similar conditions, implying that great part of the available energy is being released as sensible heat, heating the burner or the gases surrounding the flame.

References

[1] J. Hansen, M. Sato, R. Ruedy, A. Lacis, V. Oinas, Global warming in the twenty-first century: an alternative scenario, Proc. Natl. Acad. Sci. U.S.A. 97 (2000) 9875–9880.
[2] H. Wang, Formation of nascent soot and other condensed-phase materials in flames, Proc. Combust. Inst. 33 (2011) 41–67.
[3] C.R. Shaddix, T.C. Williams, L.G. Blevins, R.W. Schefer, G. Nathan, Flame structure of steady and pulsed sooting inverse jet diffusion flames, Proc. Combust. Inst. 30 (2005) 1501–1508.
[4] J. Friend, The Chemistry of Combustion. Gurney & Jackson, 1922.
[5] S. Burke, T. Schumann, Diffusion flames, Ind. Eng. Chem. 20 (1928) 998–1004.
[6] K.-T. Wu, R. Essenhigh, Mapping and structure of inverse diffusion flames of methane, Proc. Combust. Inst. 20 (1984) 1925–1932.
[7] E.J. Lee, K.C. Oh, H.D. Shin, Soot formation in inverse diffusion flames of diluted ethene, Fuel 84 (2005) 543–550.
[8] C.R. Kaplan, K. Kailasanath, Flow-field effects on soot formation in normal and inverse methane-air diffusion flames, Combust. Flame 124 (2001) 275–294.
[9] L.G. Blevins, R.A. Fletcher, B.A. Benner, E.B. Steel, G.W. Mulholland, The existence of young soot in the exhaust of inverse diffusion flames, Proc. Combust. Inst. 29 (2002) 2325–2333.
[10] M.A. Mikofski, T.C. Williams, C.R. Shaddix, L.G. Blevins, Flame height measurement of laminar inverse diffusion flames, Combust. Flame 146 (2006) 63–72.
[11] M.A. Mikofski, T.C. Williams, C.R. Shaddix, A.C. Fernandez-Pello, L.G. Blevins, Structure of laminar sooting inverse diffusion flames, Combust. Flame 149 (2007) 463–478.
[12] K.T. Macko, L.G. Blevins, R.W. Davis, Laser Extinction in Laminar Inverse Diffusion Flames, Combust. Process. Lab, UC Berkeley, 2005.

[13] R. Demarco, F. Nmira, J.-L. Consalvi, Influence of thermal radiation on soot production in laminar axisymmetric diffusion flames, J. Quant. Spectrosc. Radiat. Transf. 120 (2013) 52–69.

[14] Y. Jung, K.C. Oh, C. Bae, H.D. Shin, The effect of oxygen enrichment on incipient soot particles in inverse diffusion flames, Fuel 102 (2012) 199–207.

[15] W.C. Reynolds, The element potential method for chemical equilibrium analysis: implementation in the interactive program STANJAN. Stanford University, 1986.

[16] R.J. Santoro, T.T. Yeh, J.J. Horvath, H.G. Semerjian, The transport and growth of soot particles in laminar diffusion flames, Combust. Sci. Technol. 53 (1987) 89–115.

[17] S. Turns, An introduction to Combustion: Concepts and Applications, McGraw-Hill, 2000.

[18] T.P. Jenkins, R.K. Hanson, Soot pyrometry using modulated absorption/emission, Combust. Flame 126 (2001) 1669–1679.

[19] P.A. Berg, D.A. Hill, A.R. Noble, G.P. Smith, J.B. Jeffries, D.R. Crosley, Absolute CH concentration measurements in low-pressure methane flames: comparisons with model results, Combust. Flame 121 (2000) 223–235.

[20] B.C. Ko, K.-H. Cheong, J.-Y. Nam, Fire detection based on vision sensor and support vector machines, Fire Saf. J. 44 (2009) 322–329.

[21] E.O. Åkesson, K.J. Daun, Parameter selection methods for axisymmetric flame tomography through Tikhonov regularization, Appl. Opt. 47 (2008) 407.

[22] C.J. Dasch, One-dimensional tomography: a comparison of Abel, onion-peeling, and filtered backprojection methods, Appl. Opt. 31 (1992) 1146–1152.

[23] K.J. Daun, K.A. Thomson, F. Liu, G.J. Smallwood, Deconvolution of axisymmetric flame properties using Tikhonov regularization, Appl. Opt. 45 (2006) 4638.

[24] P.C. Hansen, Analysis of discrete ill-posed problems by means of the L-Curve, SIAM 34 (1992) 561–580.

[25] W.H. Dalzell, A.F. Sarofim, Optical constants of soot and their application to heat-flux calculations, J. Heat Transf. 91 (1969) 100–104.

[26] H. Chang, T.T. Charalampopoulos, Determination of the wavelength dependence of refractive indices of flame soot, Proc. R. Soc. A Math. Phys. Eng. Sci. 430 (1990) 577–591.

[27] L.H. Liu, J. Jiang, Inverse radiation problem for reconstruction of temperature profile in axisymmetric free flames, J. Quant. Spectros. Radiat. Transf. 70 (2001) 207–215.

[28] R. Henríquez, R. Demarco, J.-L. Consalvi, F. Liu, A. Fuentes, The oxygen index on soot production in propane diffusion flames, Combust. Sci. Technol. 186 (2014) 504–517.

[29] A. Fuentes, G. Legros, H. El-Rabii, J.-P. Vantelon, P. Joulain, J.L. Torero, Laser-induced incandescence calibration in a three-dimensional laminar diffusion flame, Exp. Fluids 43 (2007) 939–948.

[30] F. Liu, D.R. Snelling, K.A. Thomson, G.J. Smallwood, Sensitivity and relative error analyses of soot temperature and volume fraction determined by two-color LII, Appl. Phys. B Lasers Opt. 96 (2009) 623–636.

[31] O. Angrill, H. Geitlinger, T. Streibel, R. Suntz, H. Bockhorn, Influence of exhaust gas recirculation on soot formation in diffusion flames, Proc. Combust. Inst. 28 (2000) 2643–2649.

[32] R. Bryant, C. Womeldorf, E. Johnsson, T. Ohlemiller, Radiative heat flux measurement uncertainty, Fire Mater. 27 (2003) 209–222.